Journal of Alloys and Compounds 514 (2012) 220–233

Contents lists available at SciVerse ScienceDirect

Journal of Alloys and Compounds

journal homepage: www.elsevier.com/locate/jallcom

Electron microscopy studies of the age-hardening behaviors in 6005A alloy and microstructural characterizations of precipitates

Wenchao Yang[a,b,*], Lanping Huang[c], Ruirong Zhang[d], Mingpu Wang[b], Zhou Li[b], Yanlin Jia[b], Ruoshan Lei[b], Xiaofei Sheng[b]

[a] The EPSRC Centre for Innovative Manufacturing in Liquid Metal Engineering, Brunel Centre for Advanced Solidification Technology (BCAST), Brunel University, Uxbridge, Middlesex UB8 3PH, UK
[b] School of Materials Science and Engineering, Central South University, Changsha 410083, China
[c] State Key Laboratory of Powder Metallurgy, Central South University, Changsha 410083, China
[d] School of Chemistry and Chemical Engineering, Central South University, Changsha 410083, China

ARTICLE INFO

Article history:
Received 15 August 2011
Received in revised form
15 November 2011
Accepted 15 November 2011
Available online 25 November 2011

Keywords:
Aluminum alloys
High-resolution electron microscopy (HREM)
Microstructure
Precipitate
Strengthening
Moiré fringes

ABSTRACT

High-resolution electron microscopy was used to research the age-hardening behaviors in 6005A alloy and the microstructural characterizations of precipitates. It was found that β″, β′ and Q′ precipitates had 12 orientation variants, respectively, the smaller size and a high-density β″ precipitates existed in alloy for a long time, which played a very important role in controlling an anti-overaged softening behavior in 6005A alloy. Further, by the crystallographic interface and morphology analysis, a main reason was that a 2-dimensions coherency strain-field not only had the high-density β″ precipitates become the biggest obstacle of dislocations movement, but also made them transform into β′ and Q′ precipitates with more difficulty. Moreover, it was also found that β′ and Q′ precipitates had weaker relatively strain-fields, the larger size and a lower density, which were largely associated with the reduction in hardness that occurred upon overaging. Further, the strengthening of precipitates on alloys could be summarized as: β″ > Q′ > β′. Based on the structural information, the quantitative Moiré fringes analytical technique was also used to verify the lattice parameters and orientation of precipitates.

1. Introduction

As a result of medium strength, extrusion performance, good corrosion resistance and excellent welding performance, the Al–Mg–Si–Cu alloys are widely used as key materials of rail transportation and automotive industry [1]. In recent years, a number of fabrication techniques and alloying methods have been developed to research the effects on the precipitation hardening behavior and the microstructural development during artificial aging in Al–Mg–Si–Cu alloys, and further to increase the mechanical strength of alloys [2–5]. In particular, the precipitation strengthening through some metastable nano-particles precipitated from the matrix, as one of the most essential techniques, is still widely researched [6–8].

However, the precipitation process of Al–Mg–Si–Cu alloys is quite complex. In general, the precipitation sequence can be described as: supersaturated solid solution (SSSS) → cluster/GP zones → β″ → β′ + Q′ → β + Q [9–11]. The clusters and GP zones are believed to be spherical, which are aggregates of solute atoms and fully coherent with the Al matrix [12]. In the subsequent artificial aging, they can serve as nucleation sites for the β″ phases, which have the needle-shaped morphology along the $\langle 1\,0\,0\rangle_{Al}$ directions, and are considered as the main hardening precipitates in this system [13,14]. The β′ and Q′ phases, form after β″ phase in the aging sequence, and have the rod-shaped morphology along the $\langle 1\,0\,0\rangle_{Al}$ directions [7]. Moreover, the Q′ can be also known as B′ and M [15,16], or Type-C in the excess Si alloys [17]. The β and Q are the equilibrium phases in this system. They have a CaF_2 type FCC structure and a Th_7S_{12} type HCP structure, respectively [18,19]. Table 1 gives some references and more detailed data about these different precipitates [6,14,15,18–25].

It is very obvious that these precipitates should pay a very important role in the mechanical properties of Al–Mg–Si–Cu alloys. Currently, the researches about the Al–Mg–Si–Cu alloys either focus on compositions and structures of these precipitates (Table 1), or only consider the hardening behavior based on the microstructure [6–13,26]. However, the strengthening is always related with the type, interface, morphology, density and size of precipitates. So far, there are yet not any straightforward evidences and reasonable analysis about the strengthening mechanism of precipitates on alloys. And, if these issues can be not well defined, the mechanical behavior strengthened by these precipitates cannot also be

* Corresponding author. Tel.: +86 731 88830264; fax: +86 731 88876692.
E-mail address: wenchaoyang@csu.edu.cn (W. Yang).

0925-8388/$ – see front matter © 2011 Elsevier B.V. All rights reserved.
doi:10.1016/j.jallcom.2011.11.074

Table 1
Summary of different precipitates in Al–Mg–Si–Cu alloys.

Precipitates	Shape	Composition	Space group	Lattice parameters (nm)	Orientation relationships	References
Clusters/GP zones	Sphere	$Mg_{2+x}Al_{7-x-y}Si_{2+y}$	$C2/m$	$a=1.457$, $b=0.405$, $c=0.648$, $\beta=105.3^\circ$	Similarly β″ precipitates	[20,21]
β″	Needle	Mg_5Si_6	C-centered Monoclinic $C2/m$	$a=1.516$, $b=0.405$, $c=0.674$, $\beta=105.3^\circ$	$(0\,1\,0)_{\beta''}//\{1\,0\,0\}_{Al}$ $[0\,0\,1]_{\beta''}//\langle 3\,1\,0\rangle_{Al}$	[14,22]
β′	Rod or lath	Mg_9Si_5	HCP $P6_3/m$	$a=b=0.715$, $c=0.405/1.215$ $\gamma=120^\circ$	$(0\,0\,1)_{\beta'}//\{1\,0\,0\}_{Al}$ $[2\,\bar{1}\,\bar{1}\,0]_{\beta'}//\langle 3\,1\,0\rangle_{Al}$	[18,23,24]
Q′	Lath	$Al_{.38}Mg_{8.6}Si_7Cu_1$	HCP $P\bar{6}$	$a=b=1.032$, $c=0.405$, $\gamma=120^\circ$	$(0\,0\,0\,1)_{Q'}//\{0\,0\,1\}_{Al}$ $[2\,\bar{1}\,\bar{1}\,0]_{Q'}//\langle 5\,1\,0\rangle_{Al}$	[6,15,24,25]
β	Plate	Mg_2Si	FCC $Fm\bar{3}m$	$a=b=c=0.635$	$(0\,0\,1)_{\beta}//(0\,0\,1)_{Al}$ $[1\,1\,0]_{\beta}//[1\,0\,0]_{Al}$	[18]
Q	Round or oval	$Al_3Mg_9Si_7Cu_2$	HCP $P\bar{6}$	$a=b=1.039$, $c=0.402$, $\gamma=120^\circ$	Similarly Q′ precipitates	[10,19]

Table 2
Chemical composition of the Al–Mg–Si–Cu 6005A alloy.

Element	Mg	Si	Cu	Cr	Mn	Fe	Al
wt%	0.65	0.73	0.13	0.13	0.17	0.15	98.04
at%	0.72	0.70	0.06	0.07	0.08	0.07	98.29

fully understood. For instance, after the Al–Mg–Si–Cu alloys are peak-aged at quick-bake temperatures (170–190 °C), why they always present an obvious anti-overaged softening behavior which makes alloys maintained a high mechanical performance during use [10,12,27–32]? And, these reasons resulted in this behavior are still unclear.

The goal of this paper was to research the structure-property relationships of Al–Mg–Si–Cu 6005A alloy (especially, an anti-overaged softening behavior) by observing the microstructual evolution and analyzing the crystallographic interface and morphology of different precipitates using HREM and quantitative orientation characterization techniques. Finally, based on some diffraction information, the quantitative Moiré fringes analytical technique was also used to verify the lattice parameters and orientation of precipitates.

2. Experimental details

The Al–Mg–Si–Cu 6005A alloy was received in the form of extruded sheets with 5 mm thickness having the composition shown in Table 2. Prior to the heat treatment, the sheets were cut into short billets having 20 mm × 20 mm size. And then, these samples were heated at 550 °C for 1 h to obtain a complete solution of Mg, Si and Cu atoms. Following the solution treatment, samples were quenched in water at room temperature (~20 °C). Then, aging treatments were performed at 175 °C and 200 °C, respectively, to elaborate the relationships between the age-hardening behavior and microstructure.

Vickers hardness measurements (2 kg load for 15 s, five indentations per sample) were performed for each sample using a HV-5 sclerometer. A JEOL-2100F HREM operating 200 kV was used for the microstructure investigation. Transmission electron microscopy (TEM) specimens were prepared by standard electro-polishing. The electrolytic solution was a mixture of nitric acid and methyl alcohol (2:8), used at −20 °C to −30 °C and 22 V. Finally, based on the hardening curves, different conditions were selected for detailed TEM and HREM observations under the $[0\,0\,1]_{Al}$ zone axis.

Then, in order to find a correlation between the hardening behavior and the microstructure and the types of precipitates formed, these specimens for different time were examined by quantitative TEM analysis, which was conducted on 10 or more images of each sample (based on the commercial applications of the alloy, 175 °C was only considered). Bright-field (BF) images had been used to measure the length or count number of the precipitates, while dark-field images had been utilized for all precipitate-size measurements as well as for counting the number of precipitates [33]. However, except that the needle-shaped β″ precipitates with an obvious coherency stain-field are easy to distinguish, both of β′ and Q precipitates have similar the rod-shaped morphology along the $\langle 0\,0\,1\rangle_{Al}$ directions so as to distinguish them in TEM images more difficultly. Therefore, both of them are put together to measuring. To reduce the errors, the different areas were analyzed for each of the specimens at same magnifications (60,000×). And, the thickness of the observed area was estimated by counting the number of extinction fringes at an inclined grain boundary [34]. Moreover, because this thickness of samples ranged from 170 nm to 250 nm, the average value 210 ± 20 nm was used in this paper.

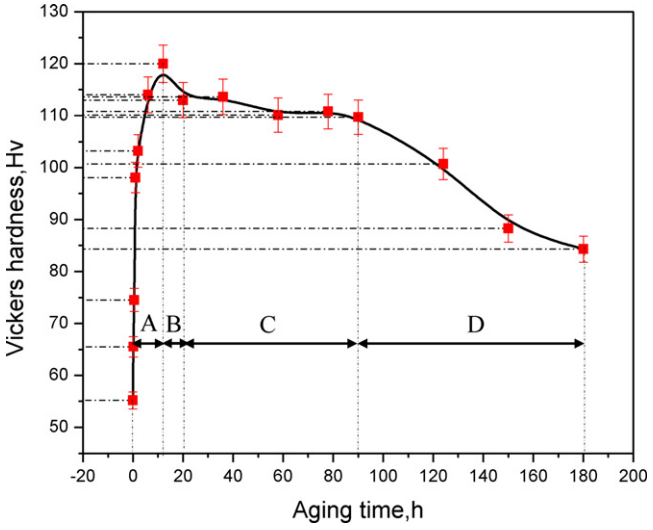

Fig. 1. Age-hardening curve of experimental alloy aging at 175 °C.

3. Results

3.1. Hardness curve, 175 °C

Fig. 1 shows a typical hardening curve aging at 175 °C of the experimental alloy, with the error bars indicating the deviations of individual measurements. The over shape of the curve largely follows the expected evolution of rapid increase in hardness followed by a hardness plateau in which the hardness has only a little decrease, but subsequent decreases rapidly. In other words, the curve can be roughly divided into four regions according to hardening response: Region A with a rapid hardening stage from 55 HV at as-quenched state to 120 HV at 12 h (peak-aged); Region B with a hardness decrease after peak-aged until 20 h; Region C with a broad hardening plateau between 113 HV and 110 HV from 20 h to 90 h; and Region D with a hardness decrease rapidly to 84 HV at 180 h. Consequently, specimens under six aging conditions in Regions A, C and D, i.e. 10 min, 30 min, 12 h, 36 h, 78 h and 150 h, were selected for further detailed microstructural observations.

3.2. Development of microstructures, 175 °C

Fig. 2 shows some BF TEM images and the corresponding $[0\,0\,1]_{Al}$ select area electron diffraction patterns (SADP) aging at 175 °C for different times. Those specimens selected for the quantitative TEM analysis and the corresponding microstructures are summarized in Table 3.

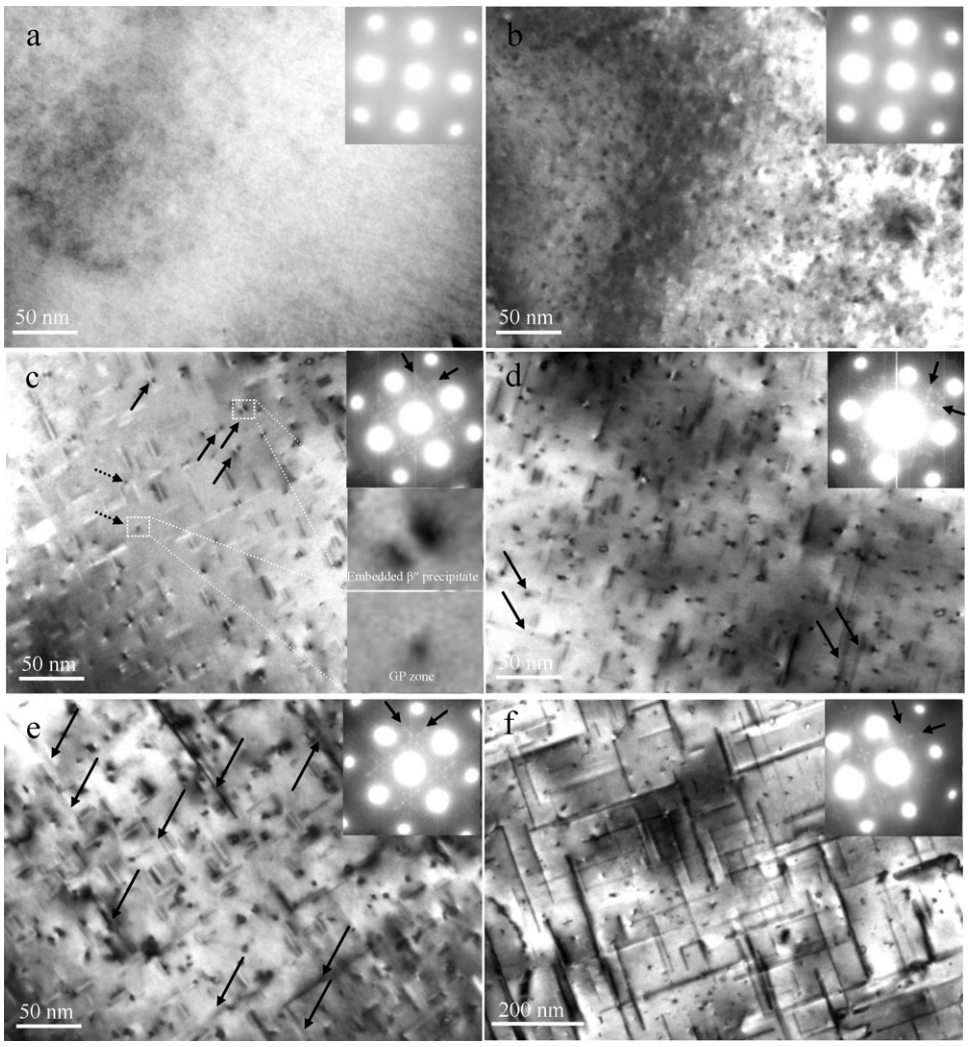

Fig. 2. BF TEM images and the corresponding $[0\,0\,1]_{Al}$ SADPs of alloy aging at 175 °C for different times. (a) 10 min, (b) 30 min, (c) 12 h, (d) 36 h, (e) 78 h, (f) 150 h. Corresponding SADPs are given as the inserts. And other inserts in Fig. 2c are two enlarged images of an embedded β″ precipitates and a GP zone, respectively. These vertical streaking observed at high-intensity reflections in SADPs are caused by overexposure of the charge-coupled device (CCD) camera.

3.2.1. Underaged microstructures

In early aging only 10 min as shown in Fig. 2a, there is no any evidence of visible precipitates, indicating that GP zones are not precipitated. However, the hardness increases to 62 HV from 55 HV at as-quenched state (Fig. 1). The result may indicate that the hardness increase at this stage should be ascribed solely to some solute atom clusters, i.e. Mg clusters, Si clusters or Mg/Si co-clusters (Table 3). However, because of the smaller size and the smaller lattice distortion resulting from very closely atomic radiuses of Al, Mg and Si, these clusters cannot display obvious strain contrast.

Upon further age-hardening to 30 min, a large number of spherical GP zones start to be precipitated evenly as shown in Fig. 2b. These spherical GP zones have only 2–4 nm size and a very high number density (Table 3), which further make the hardness increased to 75 HV.

Table 3
Number density, size and type of the precipitates aging at 175 °C for different time.

Samples investigated	Number density $\rho \times 10^3$ (μm^{-3})	Length L (nm)	Cross-section A (nm^2)	Precipitate type
175 °C/10 min	–	–	–	Clusters
175 °C/30 min	56.6	3.1	7.5[a]	GP
175 °C/12 h[b]	15.5	15.8	7.4	β″
175 °C/36 h	13.7	16.9	8.3	β″
	1.0	90.6	31.3	β′ + Q′
175 °C/78 h	11.8	19.1	9.3	β″
	1.8	122.4	42.9	β′ + Q′
175 °C/150 h	3.3	300.2	56.8	β′ + Q′

[a] The cross-section of GP can be calculated by $A = \pi(L/2)^2$.
[b] Since the GP zones are very small and have similar cross-sectional areas as β″ precipitates in each filed, they are difficultly distinguished in TEM image aging at 175 °C for 12 h and not listed in Table 3. Where the number of β″ precipitates can be counted by BF image based on their coherency stain-field.

However, note that apart from some diffraction spots from Al matrix, no any excess diffraction reflection can be observed in the SADPs of early aging stage.

3.2.2. Peak-aged microstructure

The peak-aged microstructure and the SADP are shown in Fig. 2c. Compared with that in Fig. 2b, the number density of precipitates decreases rapidly (Table 3). GP zones have transformed into the needle-shaped β″ precipitates with ~10–20 nm in length. And, these β″ precipitates are predominant in the microstructure and present some obvious coherency strain-fields surrounding the needles along the $\langle 1\,0\,0\rangle_{Al}$ directions. They are generally considered to be responsible for the maximum age-hardening effect in Al–Mg–Si–Cu alloys [13,35]. Moreover, some embedded β″ precipitates, which are aligned with the long axis parallel to the electron beam, also present some obvious Lobe-shaped coherency strain-field contrast as shown by the solid arrows. It indicates that the needle-shaped β″ precipitates may have a 2-dimensions coherency strain-field, i.e. one surrounds the needles and another surrounds its cross-section. In addition, apart from the β″ precipitates, a few spherical GP zones are also displayed in Fig. 2c, which are shown by the dashed arrows. After peak-aged, these GP zones will be dissolved into the matrix so that the hardness decreases in Region B.

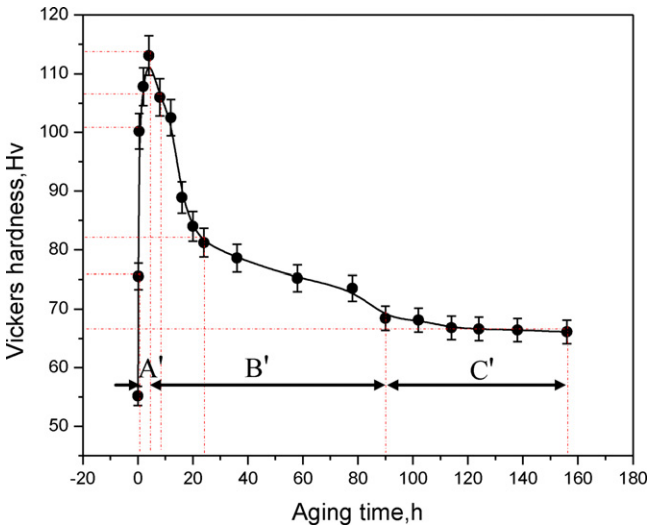

Fig. 3. Age-hardening curve of experimental alloy aging at 200 °C.

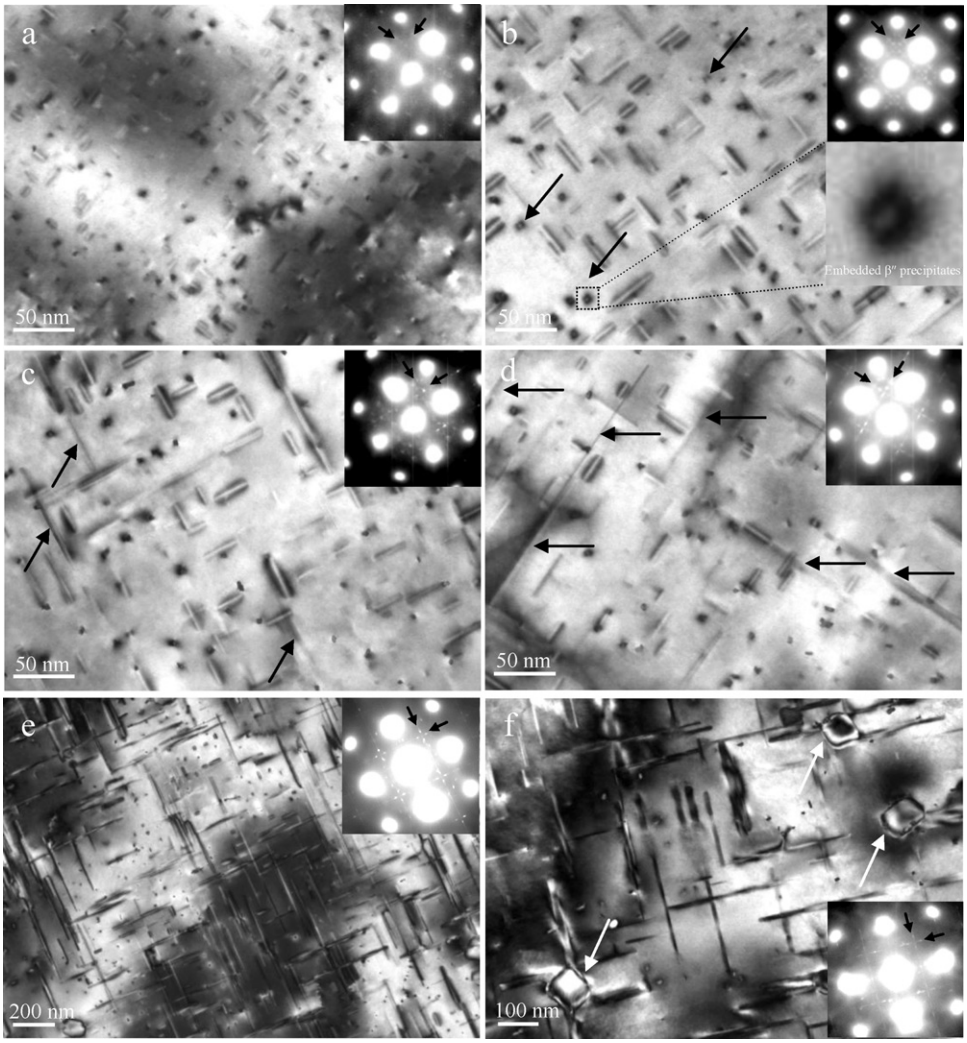

Fig. 4. BF TEM images and the corresponding $[0\,0\,1]_{Al}$ SADPs of alloy aging at 200 °C for different times. (a) 10 min, (b) 30 min, (c) 4 h, (d) 8 h, (e) 24 h, (f) 156 h. Corresponding SADPs are given as the inserts. And, other insert in Fig. 4b is an enlarged image of an embedded β″ precipitates with Lobe-shaped coherency strain-field contrast.

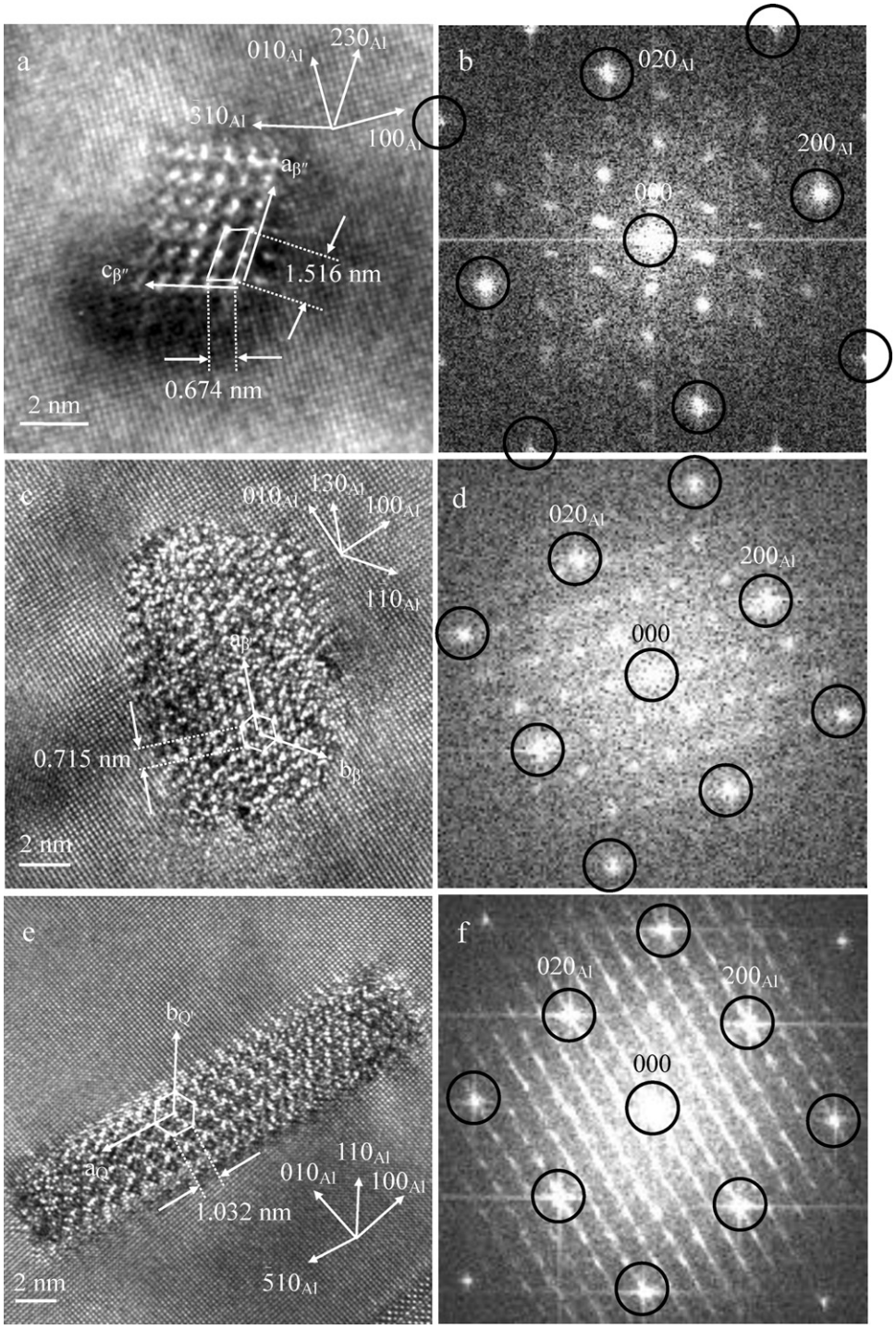

Fig. 5. HREM images and the corresponding FFT patterns of different precipitates. (a and b) β″ precipitate, (c and d) β′ precipitate, (e and f) Q′ precipitate.

Then, some "cross-shaped" diffraction streaks around $\{1\,1\,0\}_{Al}$ positions along the $\langle 1\,0\,0\rangle_{Al}$ directions are visible clearly in the SADP. The diffraction effect can be explained well: they should come from some high-order diffraction spots under the $[3\,0\,4]_{\beta''}$ and $[\bar{1}\,0\,6]_{\beta''}$ zone axes, and some double diffractions spots of β″ precipitates. Some detailed analysis can be found in our recent works [22,36].

3.2.3. Slight overaged microstructures in hardness plateau

After Region B, the hardness curve maintains an approximate hardness plateau for a long time from 20 h to 90 h in Region C, i.e. this alloy presents an obvious anti-overaged softening behavior. The microstructures and the corresponding SADPs aged for 36 h and 78 h are selected and shown in Fig. 2d and e, respectively.

As can be seen from Fig. 2d, although some rod-shaped phases with 80 nm ~100 nm in length are precipitated from the matrix as indicated by the arrows, their numbers are relatively fewer (Table 3). And, the needle-shaped β″ precipitates are still predominant in microstructure, and their sizes have also no growth obviously compared with Fig. 2c (Table 3). Generally, these rod-shaped precipitates are considered as β′ and Q′ [7,37].

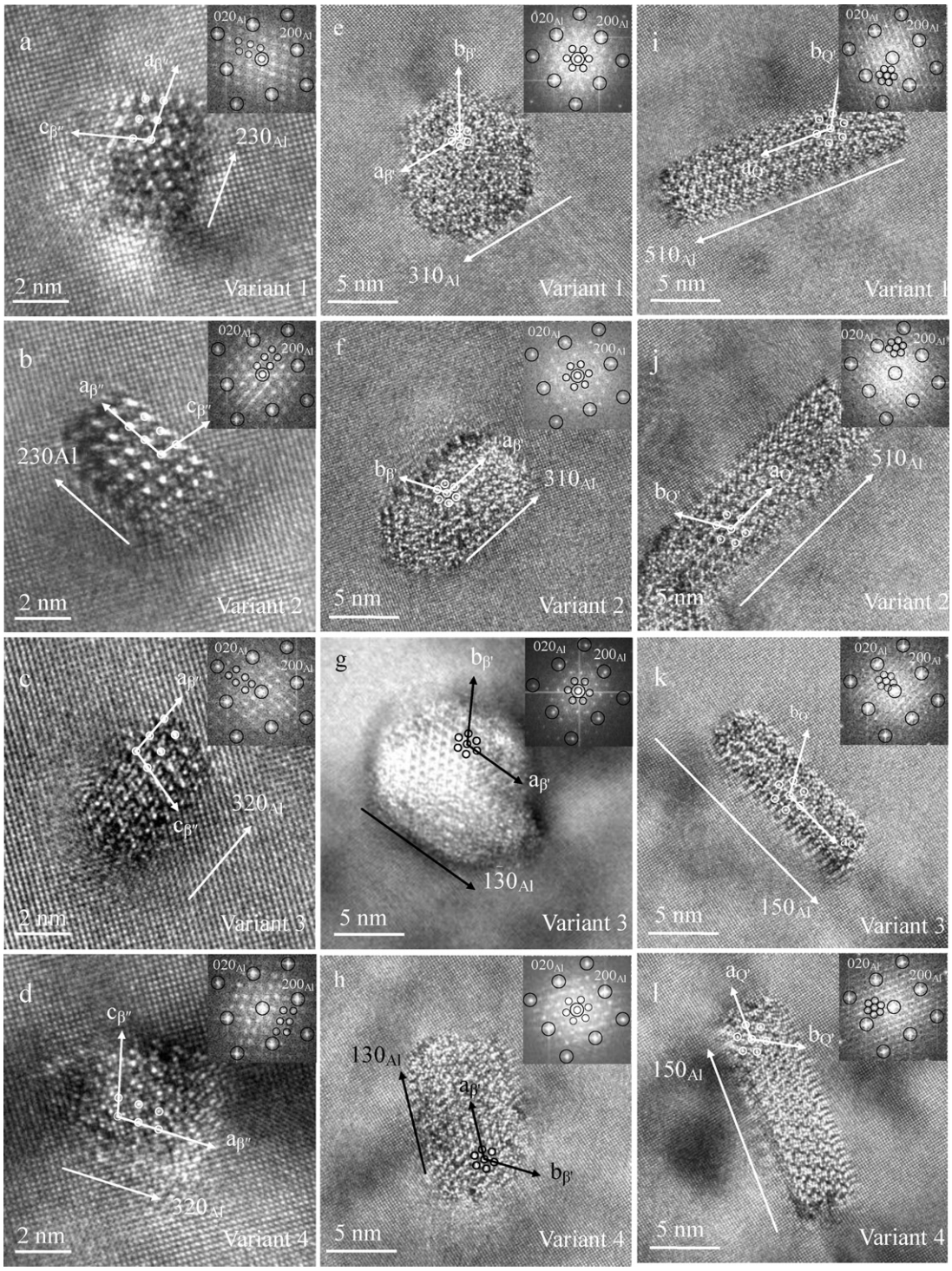

Fig. 6. HREM images of four orientation variants of precipitates on $(0\,0\,1)_{Al}$ plane. (a–d) β″ precipitates (e–h) β′ precipitates (i–l) Q′ precipitates.

Further aging to 78 h in Fig. 2e, the numbers of β″ precipitates decrease slightly, however, β″ phases are still the main precipitates in alloy (Table 3). In contrast, the numbers of these rod-shaped β′ and Q′ precipitates continue to increase, and the length has also grown up to 110–130 nm as shown by the arrows in Fig. 2e. In addition, some "cross-shaped" diffraction streaks can also be observed in SADPs of Fig. 2d and e, which are very similar to that of peak-aged stage in Fig. 2c.

3.2.4. Overaged microstructure

The microstructure and the SADP aged for 150 h are displayed in Fig. 2f. The β″ precipitates have disappeared completely and the hardness also decreases to 88 HV. And, β′ and Q′ precipitates with ~300 nm in length become predominant in Fig. 2f, but they have a lower number density in alloy (Table 3). Simultaneously, some similar "cross-shaped" diffraction streaks are also found in the SADP. They can be explained well by $[1\,4\,\bar{5}\,0]_{\beta'}$, $[5\,\bar{4}\,\bar{1}\,0]_{\beta'}$ and double

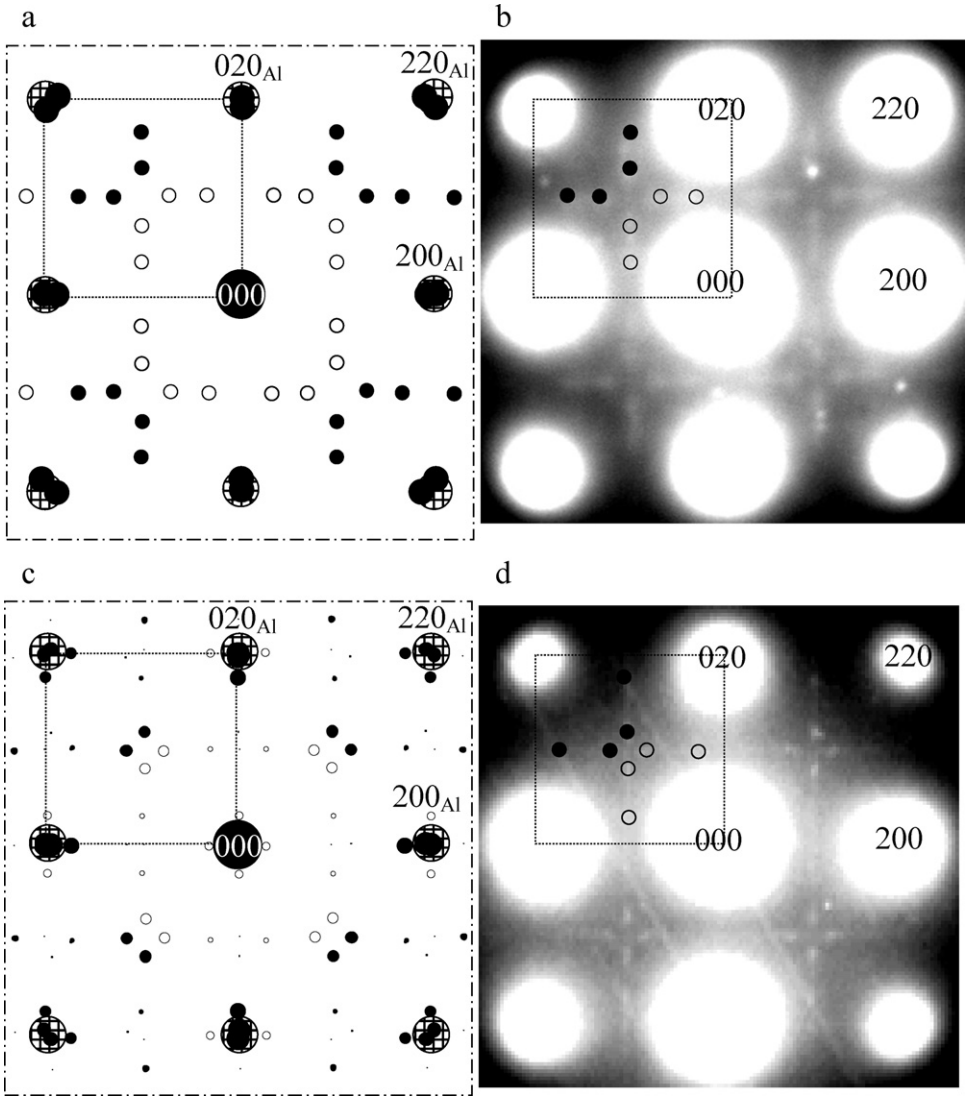

Fig. 7. Comparison of simulation and experimental $[0\,0\,1]_{Al}$ SADPs from β″ precipitates (a and b), and β′ and Q′ precipitates (c and d) at the peak-aged and the overaged stages. Open circles are the double diffractions spots. The streaking along $\langle 1\,1\,0\rangle_{Al}$ directions observed at high-intensity reflections is caused by overexposure of the CCD camera in Fig. 7b.

diffractions for β′ precipitate, together with $[1\,4\,\bar{5}\,0]_{Q'}$, $[3\,\bar{2}\,\bar{1}\,0]_{Q'}$ and double diffractions for Q′ precipitate [24].

3.3. Hardness curve, 200 °C

In order to further find a correlation between the age-hardening behavior and microstructures, an age-hardening curve of the experimental alloy at 200 °C is displayed in Fig. 3. Compared with that in Fig. 1, this curve can only be divided into three regions according to the hardening response: Region A′, B′ and C′ in Fig. 3. And, it presents a very obvious overaged softening effect (i.e. the hardness decreases rapidly in overaged stage), and an earlier peak-aged time ~4 h and a lower peak hardness ~113 HV. Consequently, specimens aging for 10 min, 30 min, 4 h, 8 h, 24 h and 156 h were selected for TEM observations.

3.4. Development of microstructures, 200 °C

Some BF TEM images and the corresponding $[0\,0\,1]_{Al}$ SADPs aging at 200 °C for different times are shown in Fig. 4. And, some "cross-shaped" diffraction streaks can also be observed under all aging conditions.

3.4.1. Underaged microstructures

In the early aging only 10 min (Fig. 4a), in addition to some spherical GP zones, a few needle-shaped β″ phases with ~12 nm in length have been precipitated. Further aging to 30 min (Fig. 4b), β″ phases grow up to ~40 nm in length and become the predominant precipitates. It indicates that the grown speed of β″ phases has been improved obviously when the aging temperature increases to 200 °C. Moreover, some Lobe-shaped strain-field contrast from some embedded β″ precipitates can also be observed as shown by the arrows in Fig. 4b.

3.4.2. Peak-aged microstructure

Aging to 4 h (i.e. peak-aged stage) in Fig. 4c, in addition to lots of β″ precipitates, a few rod-shaped β′ and Q′ precipitates with ~80 nm to 100 nm in length can be also observed as shown by the arrows. It indicates that the phase transformation from β″ precipitates to β′ and Q′ precipitates has occurred at peak-aged stage at 200 °C.

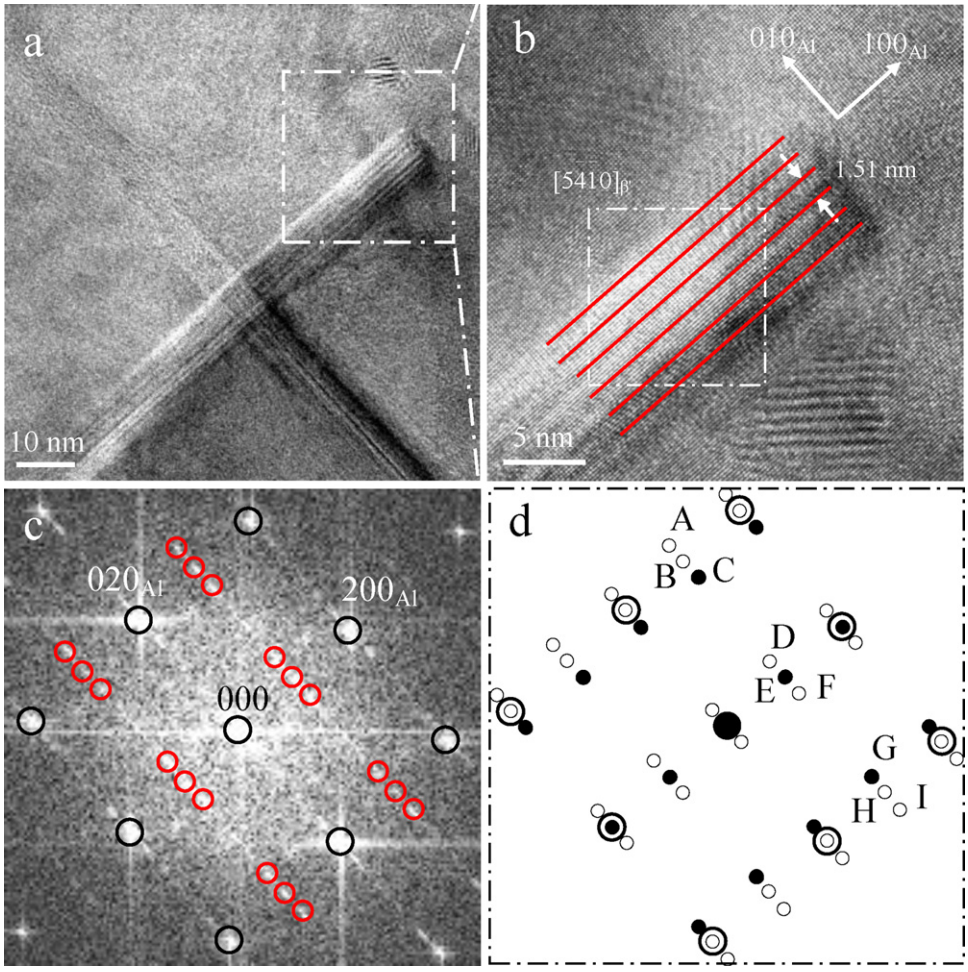

Fig. 8. Moiré fringes analysis of the β′ precipitate lying on $(0\,0\,1)_{Al}$ plane. HREM image; (b) enlarged image from rectangle area in (a); (c) Corresponding FFT patterns of rectangle area in (b); (d) simulated diffraction patterns. The Moiré fringes are parallel to the $[1\,0\,0]_{Al}$ direction. The average spacing of fringes is measured to be 1.51 nm.

3.4.3. Overaged microstructures

The overaged microstructures at 8 h, 24 h and 156 h are displayed in Fig. 4d–f, respectively. It is noticeable that β″ precipitates disappear rapidly from 8 h to 24 h, whereas the rod-shaped β′ and Q′ precipitates increase gradually, at the same time their sizes also grow up rapidly to ~350 nm in Fig. 4e. Aging to 156 h, although β′ and Q′ precipitates are still predominant in microstructure, some plate-shaped equilibrium β phases have been observed as indicated by the white arrows in Fig. 4f.

Based on the analyses above, we find that both of the phase transformation and grown speeds of precipitates in experimental alloy are improved obviously with aging temperature increased from 175 °C to 200 °C. Then, the anti-overaged softening behavior is not only related to the types of precipitates formed in alloy (especially β″ precipitates, which can maintain for a long time at 175 °C but disappeared rapidly at 200 °C), but also refers to the number density and size of precipitates. This behavior will be examined carefully by analyzing the interfaces and morphologies of precipitates in the following sections.

3.5. HREM images of precipitates

Fig. 5a–f further show the HREM images and the corresponding fast Fourier filtering transform (FFT) patterns of three main precipitates (β″, β′ and Q′), respectively, where the electron beam is parallel to $[0\,0\,1]_{Al}$ direction. And, the {2 0 0} lattices of Al matrix are used to calibrate the magnification of the microscope.

A typical HREM image of an embedded β″ precipitate is shown in Fig. 5a and b is the corresponding FFT patterns. They clearly present the unit cell structure and orientation relationships of β″ precipitate: C-centered monoclinic structure with $a = 1.516$ nm, $c = 0.674$ nm and $\beta = 105.26°$; $(0\,1\,0)_{\beta''}//(0\,0\,1)_{Al}$, $[1\,0\,0]_{\beta''}//[2\,3\,0]_{Al}$ and $[0\,0\,1]_{\beta''}//[\bar{3}\,1\,0]_{Al}$. And, because β″ precipitates lying on $(0\,0\,1)_{Al}$ plane show fully coherency along the b-axis, the parameter of the b-axis can be confirmed to be about 0.405 nm [14].

HREM images and the corresponding FFT patterns of β′ and Q′ precipitates are shown in Fig. 5c–f, respectively. Both have the same HCP structure but different lattice parameters: $a = b = 0.715$ nm, $\gamma = 120°$ for the β′ precipitate, and $a = b = 1.032$ nm, $\gamma = 120°$ for Q′ precipitate. And, the β′ precipitate has $\{3\,1\,0\}_{Al}$ habit planes but $\{5\,1\,0\}_{Al}$ habit planes for Q′ precipitate. Further, the orientation relationships can be found to be: $(0\,0\,0\,1)_{\beta'}//(0\,0\,1)_{Al}$, $[2\,\bar{1}\,\bar{1}\,0]_{\beta'}//[1\,3\,0]_{Al}$ and $[\bar{1}\,2\,\bar{1}\,0]_{\beta'}//[1\,\bar{1}\,0]_{Al}$ for β′ precipitate, and $(0\,0\,0\,1)_{Q'}//(0\,0\,1)_{Al}$, $[2\,\bar{1}\,\bar{1}\,0]_{Q'}//[\bar{5}\,1\,0]_{Al}$ and $[\bar{1}\,2\,\bar{1}\,0]_{Q'}//[1\,1\,0]_{Al}$ for Q′ precipitate.

4. Discussion

4.1. Orientation variants and diffraction patterns

Based on these orientation relationships obtained in section 3.5, three main precipitates (β″, β′ and Q′) may be precipitated along any one of four $\langle u\,v\,0\rangle_{Al}$ directions on $(0\,0\,1)_{Al}$ plane, which can

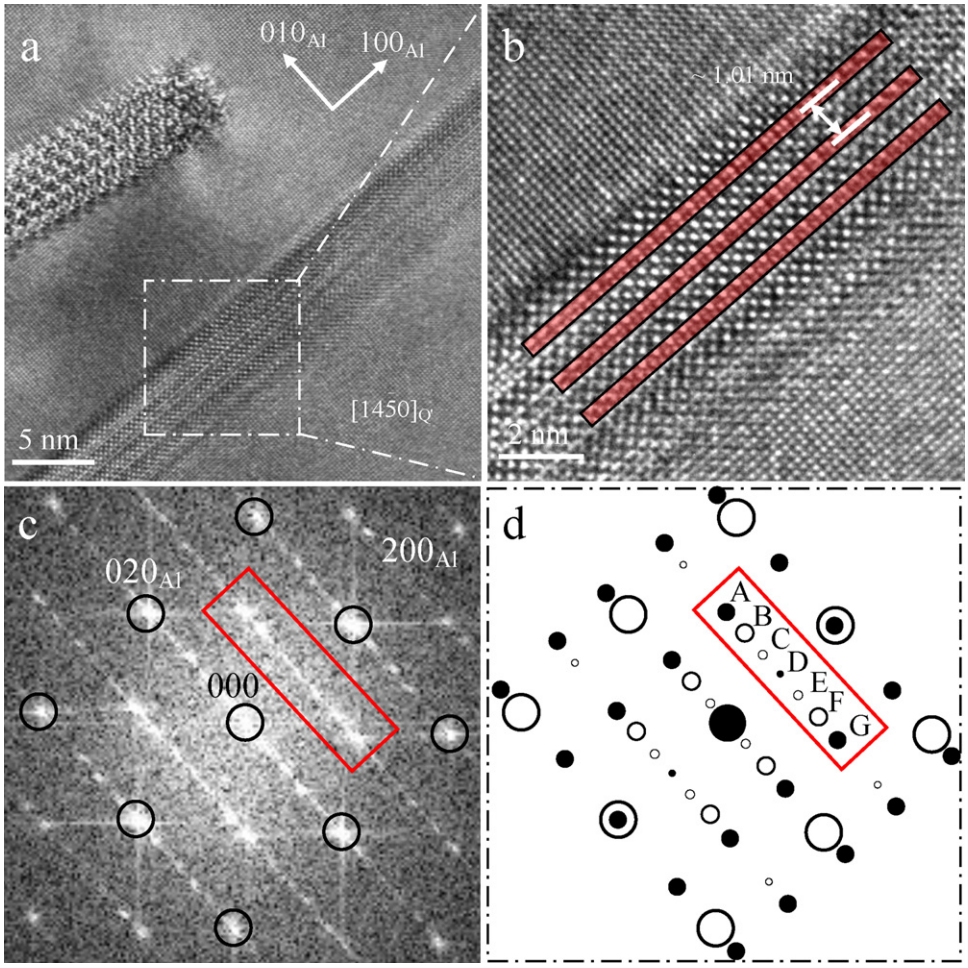

Fig. 9. Moiré fringes analysis of the Q′ precipitate lying on $(0\,0\,1)_{Al}$ plane. HREM image; (b) Enlarged image from rectangle area in (a); (c) corresponding FFT patterns of rectangle area in (b); (d) simulated diffraction patterns. The Moiré fringes are parallel to the $[1\,0\,0]_{Al}$ direction. The average spacing of fringes is measured to be 1.01 nm.

further give four orientation variants, respectively. Therefore, Fig. 6 shows the HREM images of four orientation variants of β″, β′ and Q′ precipitates along different directions on $(0\,0\,1)_{Al}$ plane.

Further considering three $\{1\,0\,0\}_{Al}$ planes of the matrix, all precipitates may yield a total of 12 orientation variants when they are precipitated from the matrix. All of orientation relationships, therefore, should be described as: $(0\,1\,0)_{\beta''}//\{1\,0\,0\}_{Al}$; $[0\,0\,1]_{\beta''}//\langle 3\,1\,0\rangle_{Al}$; $[1\,0\,0]_{\beta''}//\langle 2\,3\,0\rangle_{Al}$ for β″ precipitates; $(0\,0\,0\,1)_{\beta'}//\{1\,0\,0\}_{Al}$, $[2\,\bar{1}\,\bar{1}\,0]_{\beta'}//\langle 3\,1\,0\rangle_{Al}$ and $[\bar{1}\,2\,\bar{1}\,0]_{\beta'}//\langle 1\,1\,0\rangle_{Al}$ for β′ precipitates; $(0\,0\,0\,1)_{Q'}//\{0\,0\,1\}_{Al}$, $[2\,\bar{1}\,\bar{1}\,0]_{Q'}//\langle 5\,1\,0\rangle_{Al}$ and $[\bar{1}\,2\,\bar{1}\,0]_{Q'}//\langle 1\,1\,0\rangle_{Al}$ for Q′ precipitates, respectively.

Based on the 12 orientation variants, two different diffraction patterns models of peak-aged and overaged stages can be obtained as shown in Fig. 7. They indicate that no matter which phases (β″, β′ and Q′) are precipitated from the matrix at peak-aged or overaged stage, some "cross-shaped" diffraction streaks will always be observed inevitably under the $[0\,0\,1]_{Al}$ SADP. More detailed descriptions about the diffraction patterns analyses can be found in our recent works [22,24,36].

However, note that the "cross-shaped" diffraction streaks from Q′ precipitates have shorter separation and stronger intensity than those from β″ precipitates, and the diffraction streaks from β′ precipitates were basically overlapped with those from β″ precipitates under the $[\bar{1}\,0\,6]_{\beta''}$ zone axis [22,24]. Therefore, the evolution of precipitates may be semi-quantitative described by the diffraction information (size and intensity) together with their different morphologies (needle-shaped, rob-shaped and lath-shaped), which will be discussed in our following works.

4.2. Moiré fringes analysis

For some β′ and Q′ precipitates lying on $(0\,0\,1)_{Al}$ plane, some Moiré fringes can always be found in HREM images as shown in Figs. 8 and 9. Generally, the spacing of Moiré fringes formed by diffraction vectors g_1 and g_2 is given as $1/|\Delta g|$, and the direction of the fringes is normal to the Δg direction. Here, $\Delta g = g_1 - g_2$ [38].

In the recent works [24], we have found that β′ and Q′ precipitates with 12 orientation variants can only be precipitated along one of $[0\,0\,0\,1]_{\beta'}$, $[1\,4\,\bar{5}\,0]_{\beta'}$ and $[5\,\bar{4}\,\bar{1}\,0]_{\beta'}$ zone axes and one of $[0\,0\,0\,1]_{Q'}$, $[1\,4\,\bar{5}\,0]_{Q'}$ and $[3\,\bar{2}\,\bar{1}\,0]_{Q'}$ zone axes, respectively. Figs. 8a and 9a give the HREM images recorded from β′ and Q′ precipitate at the $[5\,\bar{4}\,\bar{1}\,0]_{\beta'}$ zone axis and $[1\,4\,\bar{5}\,0]_{Q'}$ zone axis, respectively. Based on their diffraction information, therefore, the observed spacings and orientations of the Moiré fringes can be described quantitatively by reference to Table 4. In addition, the diffraction patterns of β′ and Q′ precipitates are also given to indicate these Moiré fringes and orientation relationships.

The HREM image in Fig. 8a presents some fringes along $\langle 1\,0\,0\rangle_{Al}$ directions through precipitates. And, Fig. 8b is an enlarged image of the rectangular area in Fig. 8a, which gives clearly about 1.51 nm spacing. The corresponding FFT pattern from the rectangular area in Fig. 8b is shown in Fig. 8c. By quantitatively analyzing in Table 4, the spacings of the $\bar{1}\,\bar{2}\,\bar{3}\,\bar{0}_{\beta'}/0\,2\,0_{Al}$ and $\bar{1}\,\bar{2}\,\bar{3}\,\bar{2}_{\beta'}/2\,2\,0_{Al}$ Moiré fringes

Table 4
Spacings and directions of the Moiré fringes for β′ and Q′ precipitates. The lattice parameters $a = b = 0.715$ nm, $c = 0.405$ nm, $\gamma = 120^\circ$ for β′ precipitate, and $a = b = 1.032$ nm, $c = 0.405$ nm, $\gamma = 120^\circ$ for Q′ precipitate were used for calculations.

Precipitates	Zone axis	Set of g vectors	Corresponding plane spacing (nm)	Moiré fringes (nm)	Angle from 200_{Al} (°)	Diffraction patterns
β′	$[5\bar{4}\bar{1}0]_{\beta'}//[001]_{Al}$	$\bar{1}\bar{2}30_{\beta'}/020_{Al}$	$d_{\bar{1}\text{-}230\beta'} = 0.234$ $d_{020Al} = 0.203$	1.532	0	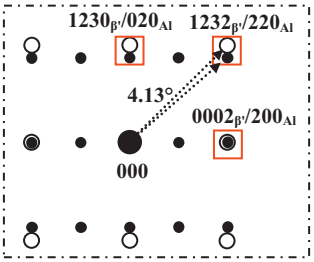
		$0002_{\beta'}/200_{Al}$	$d_{0002\beta'} = 0.203$ $d_{200Al} = 0.203$	∞	90	
		$\bar{1}\bar{2}32_{\beta'}/220_{Al}$	$d_{\bar{1}\text{-}232\beta'} = 0.153$ $d_{220Al} = 0.143$	1.496	0	
Q′	$[14\bar{5}0]_{Q'}//[001]_{Al}$	$6\bar{4}\bar{2}0_{Q'}/020_{Al}$	$d_{6\text{-}4\text{-}20Q'} = 0.169$ $d_{200Al} = 0.203$	1.009	0	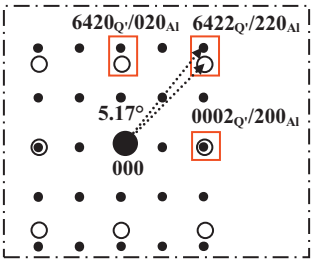
		$0002_{Q'}/200_{Al}$	$d_{000\text{-}2Q'} = 0.203$ $d_{020Al} = 0.203$	∞	90	
		$6\bar{4}\bar{2}2_{Q'}/220_{Al}$	$d_{6\text{-}4\text{-}22Q'} = 0.130$ $d_{220Al} = 0.143$	1.039	0	

are very close (i.e. 1.532 nm and 1.496 nm), and they are parallel to the $[200]_{Al}$ direction. Therefore, these two fringes may be indistinguishable in HREM image. In fact, the observed spacing of 1.51 nm in Fig. 8b should fall in between the two values in Table 4. Then, considering the double diffraction effect, a simulated diffraction pattern of Fig. 8c can be obtained in Fig. 8d, which is in good agreement with Fig. 8c. Where the labeled A, B, D, F, H and I are the results of double diffraction between β′ precipitate and Al matrix, and the labeled C, E and G are $123\bar{3}1_{\beta'}$, $0001_{\beta'}$ and $\bar{1}\bar{2}31_{\beta'}$ diffraction spots, respectively. What is more, this result may indicate that the c-axis parameter of β′ precipitate should be 0.405 nm rather than 1.215 nm [23].

Fig. 9b is an enlarged image of the rectangular area in Fig. 9a. The corresponding FFT pattern of Q′ precipitate is given in Fig. 9c. As can be seen from Table 4, the spacings of the $6\bar{4}\bar{2}0_{Q'}/020_{Al}$ and $6\bar{4}\bar{2}2_{Q'}/220_{Al}$ Moiré fringes are also very close (i.e. 1.009 nm and 1.039 nm). Therefore, the observed spacing of 1.01 nm in Fig. 9b should fall in between the two values in Table 4 and then the HREM image presents only a single set of fringes. Similarly, based on Table 4 and considering the double diffraction, a simulated diffraction pattern is given in Fig. 9d, which is also in excellent agreement with Fig. 8c. Where the labeled A, D and G represent $32\bar{1}1_{Q'}$, $0001_{Q'}$ and $\bar{3}211_{Q'}$ diffraction spots, respectively, and the labeled B, C, E and F are the results of double diffraction between the Q′ precipitate and Al matrix.

From the evidence presented and quantitative Moiré fringes analysis above, we can verify the lattice parameters and orientation variants of β′ and Q′ precipitates. However, for β″ precipitates, since they have the needle-shaped morphology with less than 4 nm cross-section, the fringes with the smallest spacing of 4.324 nm are not observable.

4.3. Crystallographic interfaces and morphologies of precipitates

Generally, the alloy can be strengthened by the interaction of moving dislocations with the precipitates. The strain-field around a precipitate as the obstacles of dislocation movement is largest when the lattices of the precipitates are coherent or semi-coherent with matrix. In the case of an incoherent precipitate, the strain-field is small, and thus the pinning potential of this precipitate is relatively small [39]. In addition, the precipitates growth is usually bounded by a combination of coherent or semi-coherent interfaces and smoothly curved incoherent interfaces. According to the theory of interface-controlled growth [40], the precipitate with the coherent and semi-coherent interfaces has very low mobility and then is not easy to coarsening, which may result in a high number density. On the other hand, the precipitate with the incoherent interfaces is highly mobile and then easy to coarsening, giving a low number density. Therefore, knowledge of the interface and morphology of the precipitate with the matrix is essential of an understanding of the strength enhancement.

Based on the lattice parameters and orientation variants obtained above, the interfaces between the embedded precipitates and the $\{200\}_{Al}$ planes of matrix were analyzed by the crystallography and orientation relationships, the analytic data are summarized in Table 5. Furthermore, according to the observed orientation relationship along the two principal axes, the mismatch can also be calculated from a plane matching criterion as the difference in the spacing of corresponding planes, and these results are listed in Table 6.

4.4. β″ precipitate

Fig. 10a displays the HREM image of an embedded β″ precipitate, its a-axis is along the $[320]_{Al}$ direction and c-axis is along the $[1\bar{3}0]_{Al}$ direction (Variant 3). Further, Fig. 10b and c shows the corresponding FFT patterns and simulated diffraction patterns, respectively. It is found that there is a near coincidence between $403_{\beta''}$ and 020_{Al} reflections, and $601_{\beta''}$ and 200_{Al} reflections, respectively. Therefore, the interfaces between the two phases can be studied in more detail. Selecting the two sets of parallel planes and applying the Fourier filter, two filtered images are displayed in Fig. 10d and e, respectively. Where, some interface dislocations between the β″ precipitate and Al matrix can be observed as indicted by the white arrows. For example, the $(40\bar{3})_{\beta''}$ plane with a spacing 0.213 nm is parallel with the $(200)_{Al}$ plane with a spacing 0.203 nm. Therefore, the distance between interface dislocations is expected for 4.326 nm by misfit calculation in Table 5. Similarly, for $(601)_{\beta''}$ plane, there is 5.356 nm for an interface dislocation.

Table 5
Interface analysis of the embedded precipitates with Al matrix.

Precipitates	Coherency relationship with Al matrix	Corresponding plane spacing in precipitates and Al matrix (nm)	Misfit δ (%)	$D_{dislocation\ (nm)}$	Interfaces
β″	$(\bar{4}03)_{\beta''}//(200)_{Al}$	$d_{-403\beta''}=0.213$ $d_{601\beta''}=0.211$	4.81	4.326	Basically coherent
	$(601)_{\beta''}//(020)_{Al}$	$d_{200/020Al}=0.203$	3.86	5.356	
β′	$(12\bar{3}0)_{\beta'}//(200)_{Al}$	$d_{12\text{-}30\beta'}=0.234$	14.2	1.540	Semi-coherent with $(200)_{Al}$ plane and incoherent with $(020)_{Al}$ plane
	–	$d_{200Al}=0.203$	–	–	
Q′	$(14\bar{5}0)_{Q'}//(200)_{Al}$	$d_{14\text{-}50Q'}=0.195$ $d_{\text{-}6420Q'}=0.169$	4.02	4.950	Basically coherent with $(200)_{Al}$ plane and semi-coherent with $(020)_{Al}$ plane
	$(\bar{6}420)_{Q'}//(020)_{Al}$	$d_{200/020Al}=0.203$	18.3	1.018	

Table 6
Lattice correspondence for the embedded precipitates and misfit along principal axes calculated from a plane matching criterion.

Precipitates	Corresponding directions	Corresponding periodic distance in precipitates and Al matrix (nm)	Misfit δ (%)	Coherence with matrix
β″	$[100]_{\beta''}//[320]_{Al}$	$d_{100\beta''}=1.516$ $d_{001\beta''}=0.674$	3.76	Basically coherent
	$[001]_{\beta''}//[1\bar{3}0]_{Al}$	$d_{230Al}=1.460$ $d_{310Al}=0.640$	5.18	
β′	$[2\bar{1}\bar{1}0]_{\beta'}//[130]_{Al}$	$d_{2\text{-}1\text{-}10\beta'}=0.715$ $d_{01\text{-}10\beta'}=1.238$	11.07	Semi-coherent along its long-axis and incoherent along its short-axis
	$[01\bar{1}0]_{\beta'}//[3\bar{1}0]_{Al}$	$d_{310Al}=0.640$	63.68	
Q′	$[2\bar{1}\bar{1}0]_{Q'}//[\bar{5}10]_{Al}$	$d_{2\text{-}1\text{-}10Q'}=1.032$ $d_{01\text{-}10\beta'}=1.787$	<0.01	Fully coherent along its long-axis and incoherent along its short-axis
	$[01\bar{1}0]_{Q'}//[150]_{Al}$	$d_{510Al}=1.033$	53.48	

However, it is found that the distances between two phases along the $[020]_{Al}$ and $[200]_{Al}$ directions in Fig. 10 are ~6.422 nm and ~5.471 nm, which are larger than 4.326 nm and 5.356 nm, respectively. Therefore, one interface dislocation can be inserted inevitably. However, the β″ precipitate can only be observed an obvious interface dislocation in the right part, but no any interface dislocation in the left part except some slight lattice distortion (Area E) in Fig. 10e. The reason may be variation in local strain in the precipitate caused by the inside dislocations (see black arrows).

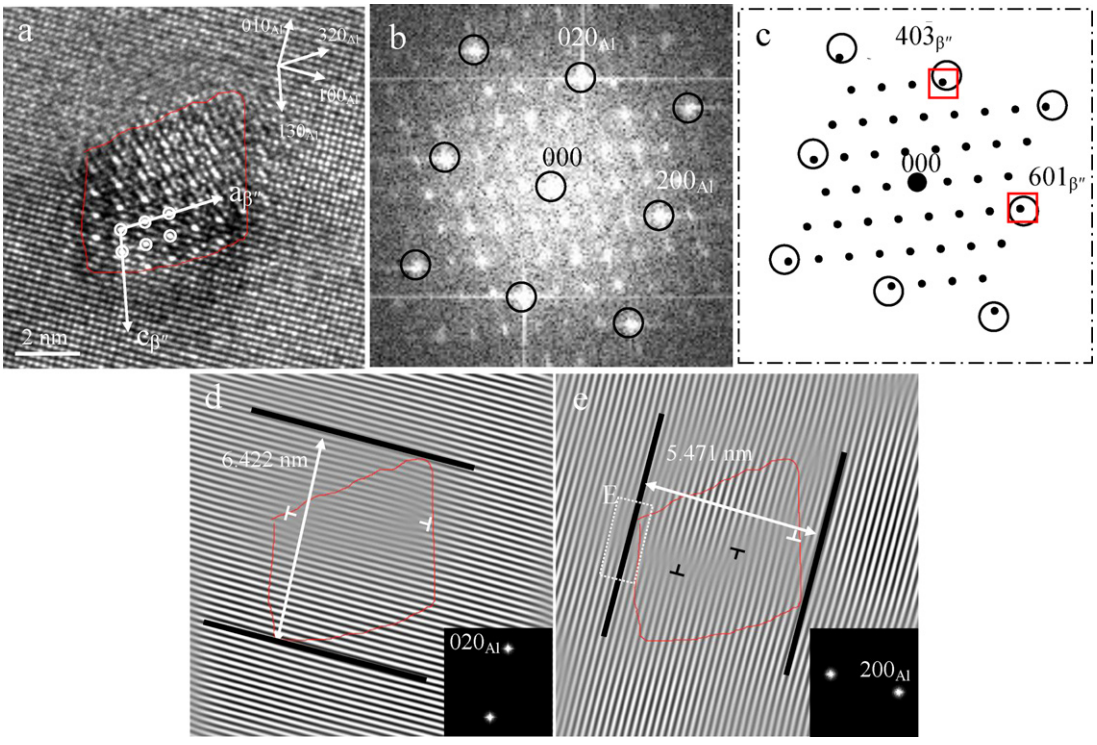

Fig. 10. Crystallographic interface and morphology analysis of the β″ precipitate. (a) HREM image; (b) corresponding FFT patterns; (c) simulated diffraction patterns; (d) IFFT image of selected 020_{Al} and $4\ 0\ \bar{3}_{\beta''}$ reflections; (e) IFFT image of selected 200_{Al} and $6\ 0\ 1_{\beta''}$ reflections.

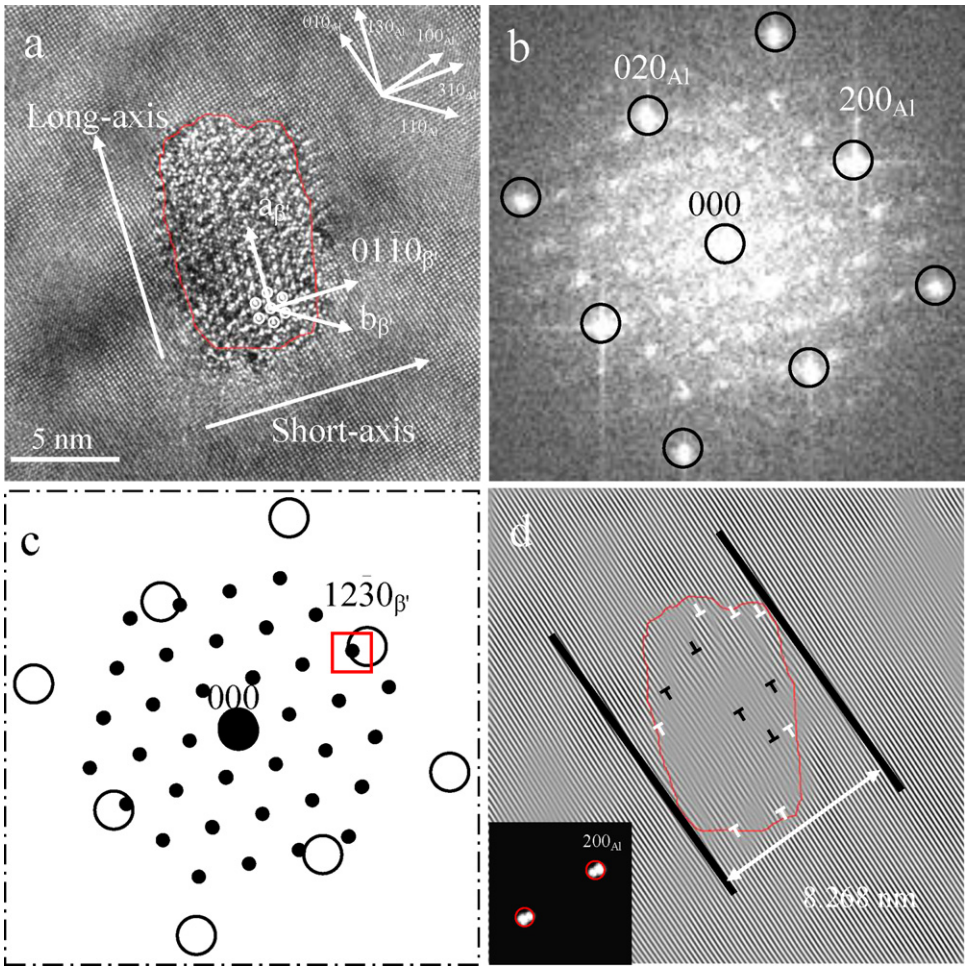

Fig. 11. Crystallographic interface and morphology analysis of the β′ precipitate. (a) HREM image; (b) corresponding FFT patterns; (c) simulated diffraction patterns; (d) IFFT image of selected $2\,0\,0_{Al}$ and $1\ 2\,\bar{3}\,0_{\beta'}$ reflections.

Simultaneously, because the embedded β″ precipitate has very small misfits (4.81% and 3.86%) with two $\{2\,0\,0\}_{Al}$ planes (see Table 5). Therefore, a lager coherency strain-field is needed to maintain the coherent interface between two phases. Only when the distance along $\langle 2\,0\,0\rangle_{Al}$ direction is larger than 4.326 nm or 5.356 nm, an interface dislocation will be inserted inevitably to decrease the total energy of the system. Then, a semi-coherent interface will become energetically more favorable to replace the coherent interface by some periodical dislocations, and further decrease the coherency strain-field around the embedded β″ precipitate. Therefore, this result indicates that, apart from the coherency strain-field around the needle, the β″ precipitate should have other coherency strain-field around its cross-section. It is in excellent agreement with the observed results in Figs. 2c and 4c.

In addition, as can be seen from Table 6, there is only 3.76% and 5.18% misfit for the β″ precipitate along the $\langle 2\,3\,0\rangle_{Al}$ and $\langle 3\,1\,0\rangle_{Al}$ direction, respectively. It indicates that the β″ precipitate has better coherency with matrix and a very low mobility along principal axes. Therefore, β″ precipitates' growth is difficult relatively so that they maintain a high number density after the peak-aged (Table 3). Moreover, because the difference between two misfits is not obvious, an approximate round cross-section may be more favorable to β″ precipitate.

4.4.1. β′ and Q′ precipitates

Fig. 11a displays the HREM image of an embedded β′ precipitate (Variant 4). And, Fig. 11b and c are the corresponding FFT patterns and the simulated diffraction patterns, respectively. It is found that there is only a set of coincident diffraction in Fig. 11c: $1\,2\,\bar{3}\,0_{\beta'}$ and $2\,0\,0_{Al}$. Therefore, the distance between interface dislocations is 1.540 nm by calculation in Table 5. However, the distance along the $[0\,2\,0]_{Al}$ direction is ~8.268 nm in Fig. 11d, which is a filtered image based on the $1\,2\,\bar{3}\,0_{\beta'}$ and $2\,0\,0_{Al}$ diffraction. Consequently, some interface dislocations will be introduced inevitably as shown by the white arrows. Simultaneity, a few inside dislocations are also observed in precipitate (see black arrows). These inside dislocations may make some strain-fields released so that the numbers of interface dislocations deviate from the theoretical calculation value.

Fig. 12a–c shows the HREM image, the corresponding FFT patterns and the simulated diffraction patterns of an embedded Q′ precipitate (Variant 1), respectively. And, the $(1\,4\,\bar{5}\,0)_{Q'}$ plane is basically coinciding with the $(0\,2\,0)_{Al}$ plane, giving a filtered image in Fig. 12d and a interface dislocation every 4.950 nm (Table 5). Simultaneity, the inside dislocations (black arrows) may also make some local strain-fields released in Q′ precipitate so that the numbers of interface dislocations (white arrow) are different from the theoretical calculation value.

Simultaneously, as can been seen from Table 5, β′ and Q′ precipitate has 14.2% and 4.02% misfit with $(2\,0\,0)_{Al}$ plane, and no lattice coherency and 18.3% misfit (i.e. $(\bar{6}\,4\,2\,0)_{Q'}//(0\,2\,0)_{Al}$) with $(0\,2\,0)_{Al}$ plane, respectively. Therefore, an embedded β′ precipitate has the semi-coherent and incoherent interfaces with Al matrix whereas basically coherent and semi-coherent interfaces for Q′ precipitate.

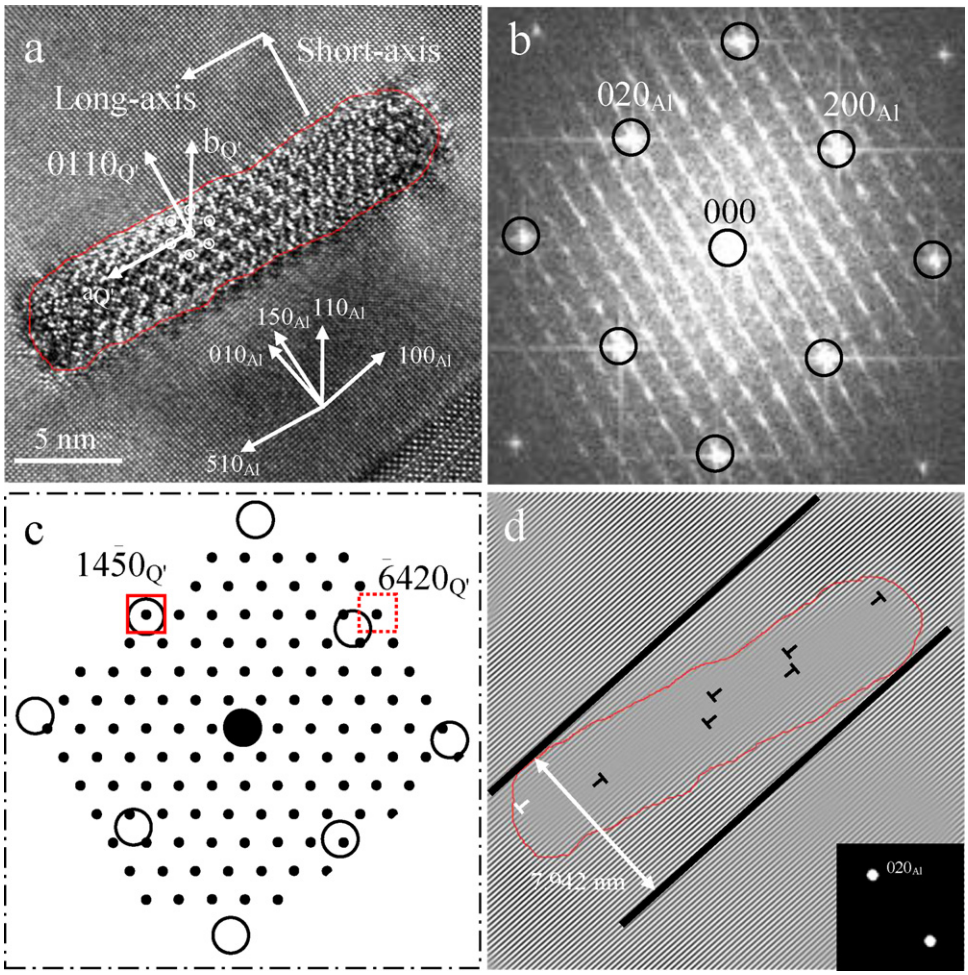

Fig. 12. Crystallographic interface and morphology analysis of the Q′ precipitate. (a) HREM image; (b) corresponding FFT patterns; (c) simulated diffraction patterns; (d) IFFT image of selected 020_{Al} and $1\ 4\bar{5}0_{Q'}$ reflections.

In other words, the strain-field around the Q′ precipitate is larger than that around the β′ precipitate. And, the more coherent Q′ precipitates will strain the matrix more compared with β′ precipitates.

Then, it is also found that there are 11.07% and 63.68% misfits for β′ precipitate in Table 6, which indicates that the β′ precipitate is semi-coherent along its long-axis and incoherent along its short-axis (Fig. 11a). Similarly, because there are less than 0.10% and 53.48% misfits for Q′ precipitate, the Q′ precipitate is fully coherent along its long-axis and incoherent along its short-axis (Fig. 12a). Therefore, both of β′ and Q′ precipitates are highly mobile and easy to coarsening along their short-axis directions, then resulting in a lower number density (Table 3). Furthermore, some lath-shaped cross-sections may be more favorable to β′ and Q′ precipitates. Furthermore, more incoherent β′ will allow the particle to grow larger in cross-section compared with Q′.

Based on the interface and morphology analyses above, a 2-dimensions coherency strain-field, the smaller size and a high number density will have β″ precipitates become the biggest obstacles of the dislocations movement. In other words, β″ precipitates can provide the maximum strengthening effect with experimental alloy in precipitation. On the other hand, β′ and Q′ precipitates have weaker relatively strain-fields, the larger size and a lower number density, therefore, their strengthening effect should be weaker than that caused by β″ precipitates. In addition, the more coherent Q′ precipitates not only strain the matrix more, but also have some smaller cross-section sizes compared with β′ precipitates. Consequently, the strengthening of three main precipitates on alloy can be described to be: β″ > Q′ > β′.

To sum up, after the peak-aged at 175 °C, β″ precipitates in experimental alloy are very difficult to happen phase transformation to β′ and Q′ precipitates (Fig. 2). Then, they still maintain some smaller size and higher number density in alloy (Table 3). Together with a 2-dimensions coherency strain-field, β″ precipitates provide the biggest lasting strengthening effects for alloy so that the hardness do not rapidly decrease at 175 °C. However, this phase transformation process is happened rapidly at 200 °C. When these β″ precipitates transforms largely into β′ and Q′ precipitates, the number density of precipitates decreases, their size increases rapidly and the strengthening on alloy weakens, which result in the hardness decreases rapidly. Therefore, the experimental alloy can present an obvious anti-overaged softening behavior at a lower temperature 175 °C but it does not exist at a higher temperature 200 °C. In addition, this result also indicates that both of β′ and Q′ precipitates should be largely associated with the reduction in hardness that occurs upon overaging.

5. Conclusions

We have used the quantitative TEM analysis and HREM technique to research the structure-property relationships in Al–0.65Mg–0.73Si–0.13Cu alloy (6005A). It is found that this alloy presents an obvious anti-overaged softening behavior at 175 °C, however, this behavior will disappear rapidly at 200 °C. Based on

the crystallographic interface and morphology analysis, the main reason is that a 2-dimensions coherency strain-field, the smaller size and a high number density have the needle-shaped β″ precipitates become the biggest obstacle of dislocations movement. Simultaneously, β″ precipitates are also very stable and not easy to transform into β′ and Q′ precipitates aging at 175 °C for a long time, but this phase transformation process will happen rapidly at 200 °C. And, because both of β′ and Q′ precipitates have relatively weaker strain-fields, the larger size and a lower density than β″ precipitates, they should be largely associated with the reduction in hardness that occurs upon overaging.

Further, the strengthening of three main precipitates on alloy can be summarized as: β″ > Q′ > β′. At the same time, it is also found that some inside dislocations exist in precipitates, which make some strain-fields released so that the numbers of interface dislocations between precipitates and Al matrix deviate from the theoretical calculation value. Moreover, β″, β′ and Q′ precipitates have 12 orientation variants with Al matrix, respectively, giving some "cross-shaped" diffraction streaks under the $[0\,0\,1]_{Al}$ SADP. Then, the Moiré fringes analytical technique is also used to verify the lattice parameters and orientation variants of precipitates.

Acknowledgments

This work is supported by the Industrialization Research Projects of National Development and Reform Commission ([1998] 1907), the Hunan Provincial Innovation Foundation for Postgraduate (CX2010B044), PR China, and the Graduate Degree Thesis Innovation Foundation of Central South University (2010ybfz024).

References

[1] W.S. Miller, L. Zhuang, J. Bottema, A.J. Wittebrood, P. De Smet, A. Haszler, A. Vieregge, Mater. Sci. Eng. A 280 (2000) 37–49.
[2] N. Tabatabaei, A. Karimi Taheri, M. Vaseghi, J. Alloys Compd. 502 (2010) 59–62.
[3] S.K. Panigrahi, R. Jayaganthan, J. Alloys Compd. 470 (2009) 285–288.
[4] A. Jaafar, A. Rahmat, Z. Hussain, I. Zainol, J. Alloys Compd. 509 (2011) 8632–8640.
[5] S. Wang, K. Matsuda, T. Kawabata, T. Yamazaki, S. Ikeno, J. Alloys Compd. 509 (2011) 9876–9883.
[6] C.D. Marioara, S.J. Andersen, T.N. Stene, H. Hasting, J. Walmsley, T.J. Van Helvoort, R. Holmestad, Philos. Mag. 87 (2007) 3385–3413.
[7] W.F. Miao, D.E. Laughlin, Metall. Mater. Trans. A 31 (2000) 361–371.
[8] A.Gaber, A.Mossad Ali, K. Matsuda, T. Kawabata, T. Yamazaki, S. Ikeno, J. Alloys Compd. 432 (2007) 149–155.
[9] K. Matsuda, Y. Uetani, T. Sato, S. Ikeno, Metall. Mater. Trans. A 32 (2001) 1293–1299.
[10] D.J. Chakrabarti, D.E. Laughlin, Prog. Mater. Sci. 49 (2004) 389–410.
[11] X. Wang, S. Esmaeili, D.J. Lloyd, Metall. Mater. Trans. A 37 (2006) 2691–2699.
[12] G.A. Edwards, K. Stiller, G.L. Dunlop, M.J. Couper, Acta Mater. 46 (1998) 3893–3904.
[13] S.K. Son, S. Matsumura, K. Fukui, M. Takeda, J. Alloys Compd. 509 (2011) 241–245.
[14] S.J. Andersen, H.W. Zandbergen, J. Jansen, C. TrÆholt, U. Tundal, O. Reiso, Acta Mater. 46 (1998) 3283–3298.
[15] S.D. Dumolt, D.E. Laughlin, J.C. Williams, Scr. Metall. 18 (1984) 1347–1350.
[16] L. Sagalowicz, G. Lapasset, G. Hug, Philos. Mag. Lett. 74 (1996) 57–66.
[17] K. Matsuda, Y. Sakaguchi, Y. Miyata, Y. Uetani, T. Sato, A. Kamio, S. Ikeno, J. Mater. Sci. 35 (2000) 179–189.
[18] M.H. Jacobs, Philos. Mag. 26 (1972) 1–13.
[19] L. Arnberg, B. Aurivillius, Acta Chem. Scand. A 34 (1980) 1–5.
[20] J.H. Chen, E. Costan, M.A. van Huis, Q. Xu, H.W. Zandbergen, Science 312 (2006) 416–419.
[21] C.D. Marioara, S.J. Andersen, J. Jansen, H.W. Zandbergen, Acta Mater. 49 (2001) 321–328.
[22] W.C Yang, M.P. Wang, R.R. Zhang, Q. Zhang, X.F. Sheng, Scr. Mater. 62 (2010) 705–708.
[23] R. Vissers, M.A. van Huis, J. Jansen, H.W. Zandbergen, C.D. Marioara, S.J. Andersen, Acta Mater. 55 (2007) 3815–3823.
[24] W.C. Yang, M.P. Wang, X.F. Sheng, Q. Zhang, L.P. Huang, Philos. Mag. Lett. 91 (2011) 150–160.
[25] M. Torsæter, W. Lefebvre, C.D. Marioara, S.J. Andersen, J.C. Walmsley, R. Holmestad, Scr. Mater. 64 (2011) 817–820.
[26] T. Abid, A. Boubertakh, S. Hamamda, J. Alloys Compd. 490 (2010) 166–169.
[27] L. Zhen, S.B. Kang, Metall. Mater. Trans. A 28 (1997) 1489–1497.
[28] S. Esmaeili, X. Wang, D.J. Lloyd, W.J. Poole, Metall. Mater. Trans. A 34 (2003) 751–763.
[29] X. Wang, W.J. Poole, S. Esmaeili, D.J. Lloyd, J.D. Embury, Metall. Mater. Trans. A 34 (2003) 2913–2924.
[30] T.E.M. Staab, R. Krause-rehberg, J. Mater. Sci. 41 (2006) 1059–1066.
[31] J. Man, L. Jing, S.G. Jie, J. Alloys Compd. 437 (2007) 146–150.
[32] W.J. Poole, X. Wang, D.J. Lloyd, J.D. Embury, Philos. Mag. 85 (2005) 3113–3135.
[33] S.J. Andersen, Metall. Mater. Trans. A 26 (1995) 1931–1937.
[34] P. Hirsch, A. Howie, R.B. Nicholson, D.W. Pashley, M.J. Whelan, in: R.E. Krieger (Ed.), Electron Microscopy of Thin Crystals, Huntington, New York, 1977.
[35] W.F. Miao, D.E. Laughlin, Scr. Mater. 40 (1999) 873–878.
[36] W.C. Yang, M.P. Wang, Y.L. Jia, R.R. Zhang, Metall. Mater. Trans. A 42 (2011) 2917–2929.
[37] A. Perovic, D.D. Perovic, G.C. Weatherly, D.J. Lloyd, Scr. Mater. 41 (1999) 703–708.
[38] T. Fujii, H. Nakazawa, M. Kato, U. Dahmen, Acta Mater. 48 (2000) 1033–1045.
[39] H.W. Zandergen, S.J. Andersen, J.##J. Jansen, Science 277 (1997) 1221–1225.
[40] M. Hillert, Metall. Mater. Trans. A 6 (1975) 5–19.